technology · applications · instrumentation
tai corporation

AXAF OPTICAL TECHNOLOGY ANALYSIS

FINAL REPORT

By

Dietrich Korsch
TAI CORPORATION
12010 S. Memorial Parkway
Huntsville, Al. 35803

Prepared for

NATIONAL AERONAUTICS AND SPACE ADMINISTRATION
MARSHALL SPACE FLIGHT CENTER, ALABAMA

Contract NAS8-33158

July 1979

P. O. Drawer B Farley Station • Huntsville, Alabama 35802 • (205) 881-4999 & 881-1272

SUMMARY

The effects of misalignment and surface deformations on the image quality of a grazing incidence telescope with six nested subsystems are investigated. The axial rms-spot size serves as measure for the image quality. The surface deformations are simulated by ellipsoidal and sinusoidal deviations from the ideal surface. Misalignments are tilts, decenters, and despaces of the individual elements. The effects of each type of defect are analyzed in a single two-element system. The full nested system is then analyzed in the presence of all possible defects on all tweleve elements, whereby the magnitude of the defects is randomized within a given upper limit.

TABLE OF CONTENTS

LIST OF FIGURES

14. Performance in the presence of linear and angular misalignments; -10^{-4} in. $\leq$ LM $\leq +10^{-4}$ in., $-5 \cdot 10^{-7}$ rad $\leq +5 \cdot 10^{-7}$ rad.

15. Performance in the presence of figure errors only; (FE) = $5 \cdot 10^{-7}$ rad.

16. Performance in the presence of figure errors only; $-5 \cdot 10^{-7}$ rad.

17. Performance in the presence of alignment and figure errors; -10^{-4} in. $\leq$ LM $\leq +10^{-4}$ in., $-5 \cdot 10^{-7}$ rad $\leq$ AM $\leq +5 \cdot 10^{-4}$ rad, $-5 \cdot 10^{-7}$ rad $\leq$ FE $\leq +5 \cdot 10^{-7}$ rad.

18. Performance in the presence of alignment and figure errors; -10^{-4} in. $\leq$ LM $\leq +10^{-7}$ in., $-5 \cdot 10^{-7}$ rad $\leq$ AM $\leq +5 \cdot 10^{-7}$ rad, (FE) = $5 \cdot 10^{-7}$ rad.

AXAF OPTICAL TECHNOLOGY ANALYSIS

Introduction

Analysis of the effects of misalignment and surface deformations on the image quality is a key part of an error budget. It is the intent of this paper to examine the sensitivities of these effects on a system characteristic of the AXAF. The axial rms-spot size serves as a measure for the image quality. The surface deformations are simulated by ellipsoidal and sinusoidal deviations from the ideal surface. Misalignments are tilts, decenters, and despaces of the individual elements. The effects of each type of defect are analyzed in a single two-element system. The full nested system is then analyzed in the presence of all possible defects on all 12 elements, whereby the magnitude of the defects is randomized within a given upper limit.

The specific results of this study are not intended to quantify these elements of the error budget, but only to understand the sensitivity. As various trade studies are performed and specific surface deformations or misalignments become known, these numbers will be used in the model and the error budget will gradually become more quantitative.

As a point of reference, the present performance goal for the AXAF is to provide a resolution of 0.5 arc seconds. The numbers used in this study are approximately compatible with that goal, but do not take into account errors due to system dynamics, aspect solution effects, or X-ray surface scattering, each of which may have significant effects on the overall performance.

Grazing Incidence Geometry

The surface equation of a conicoidal element working in grazing incidence is given by

$$\rho^2 - \rho_0^2 = 2kz - (1+\delta)z^2 \ , \quad (\rho^2 = x^2 + y^2) \ , \tag{1}$$

where ρ_0 is the central radius of the element, k is the subnormal at the center, and δ is the deformation constant (see Figure 1).

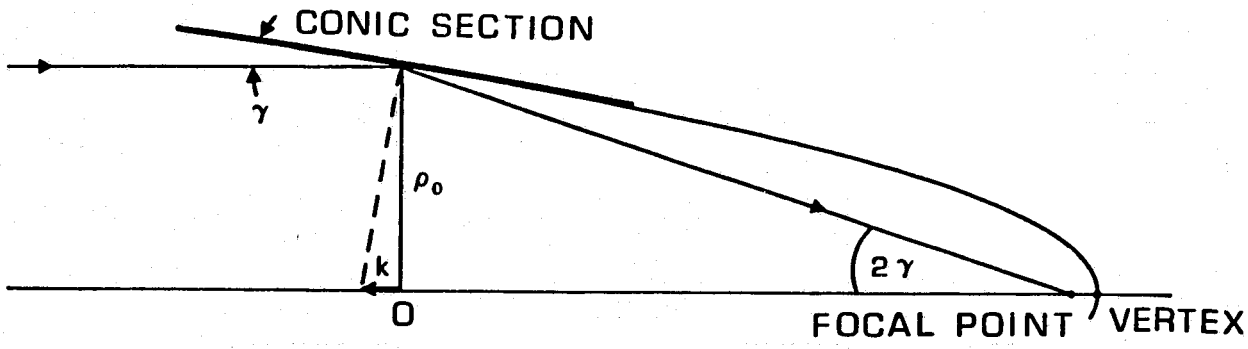

Fig. 1. Meridional section of grazing incidence surface.

The geometry of a two-mirror grazing incidence telescope as shown in Figure 2 is completely defined by the following four parameters:

Grazing Angle (at center of both elements):	γ
Center Radius of First Mirror:	ρ_{01}
Center to Center Separation:	d
Half Widths of Entrance Annulus:	$\Delta\rho$

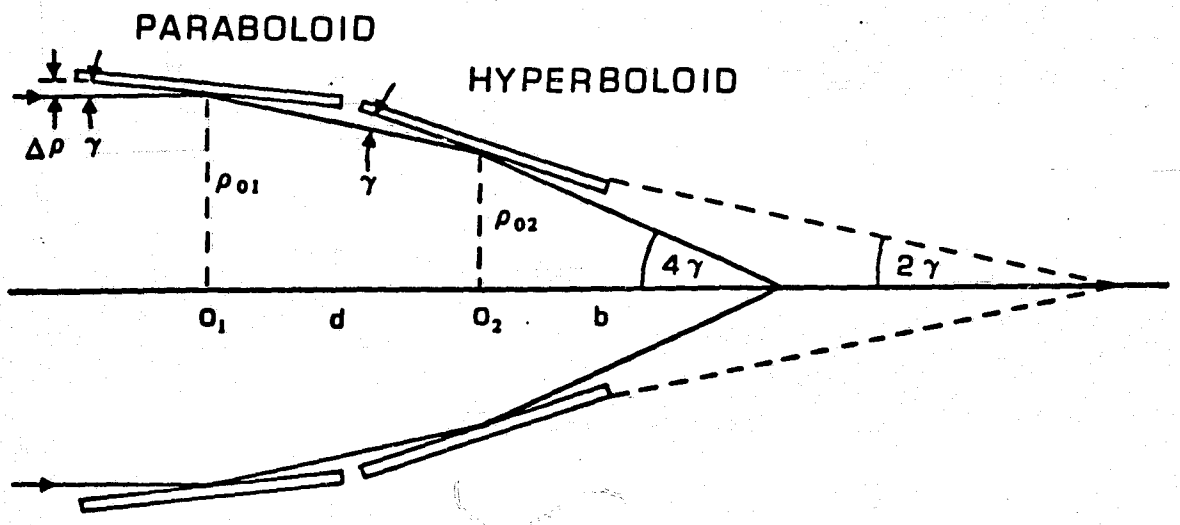

Fig. 2. Schematic of two-mirror grazing incidence telescope.

All other quantities can be expressed using only the first three input parameters. The following is a summary of the most useful system parameters and the relations among them.

Center radius of second mirror:	$\rho_{02} = \rho_{01} - d \cdot \tan 2\gamma$
Back focal distance (measured from center of second mirror):	$b = \rho_{02}/\tan 4\gamma$
Center subnormal of first surface:	$k_1 = -\rho_{01} \tan \gamma$
Center subnormal of second surface:	$k_2 = -\rho_{02} \tan 3\gamma$
Deformation constant of first surface:	$\delta_1 = -1$
Deformation constant of second surface:	$\delta_2 = -\left[\frac{\sin 2\gamma}{\sin 4\gamma - \sin 2\gamma}\right]^2$
System focal length:	$\rho_{01} \sin 4\gamma$

Figure 3 shows a projection of the entrance annulus. For the ray trace analysis described in the following, a randomized ray input grid was used in that small probability areas were assigned to the incident rays instead of a regular pattern. This avoids systematic errors that can occur, for instance, when a regular ray input grid is used to analyze periodic surface deformations.

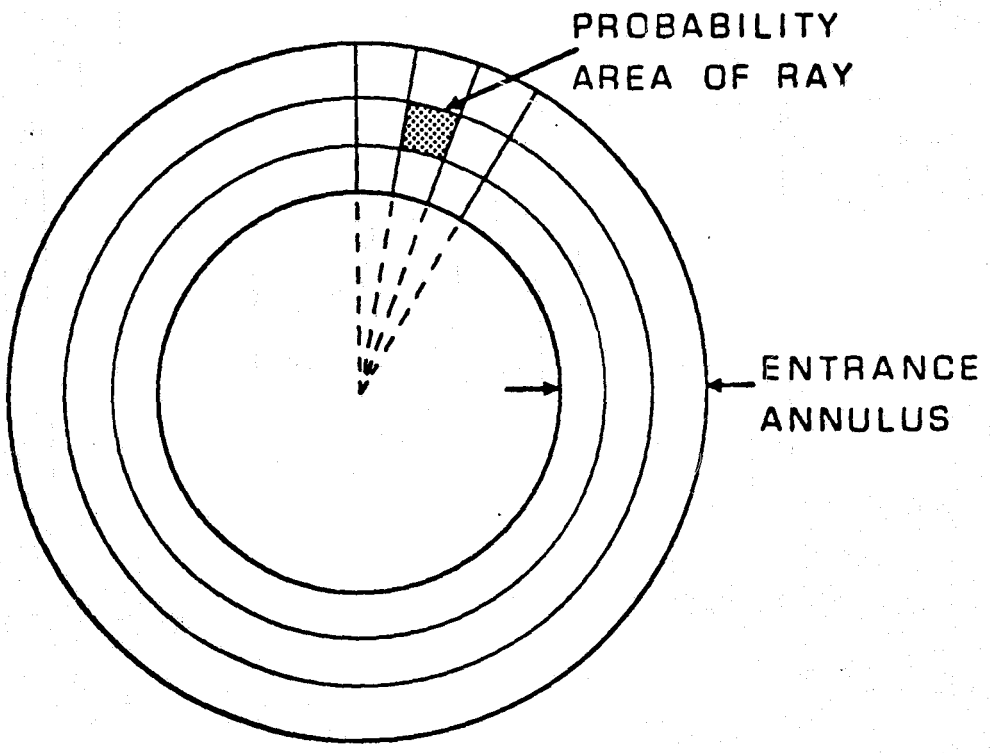

Fig. 3. Entrance annulus.

While the geometric spot size on axis of a perfect two-mirror system is zero, any real system is expected to deviate from the ideal design to a certain degree, thus introducing aberrations that can be measured as an increase of the axial spot size.

The intent of the study was to simulate as many of the expected defects as possible and determine their effects on the image quality of the telescope. Two classes of defects have benn investigated:

a) Misalignments - Misalignments are positional errors of an element with respect to a fixed system of coordinates. They are divided into two categories; linear misalignments (LM) which are displacements of an element alongg (despace) and perpendicular (decenter) to the optical axis, and angular misalignments (AM) which are tilts about the center, O, of an element in the xz- and yz-plane.

b) Figure Errors (FE) - Figure errors are deviations from the ideal surface figure. In this study only low spatial frequency errors, that is, errors causing geometric aberrations rather than scattering, are considered.

The mathematical models of various FE simulations are introduced in the next section.

A summary of all pertinent system parameters is given in Table 1.

Simulation of Figure Errors

The types of errors considered in the following are minute departures from the ideal figure, simulated mathematically by suitable modifications of the initial surface equation.

Elliptical Deformation of the Sagittal Cross-Section

a) Elliptical Deformation with Constant Azimuthal Orientation from

Table 1. System parameters

Subsystem	1	2	3	4	5	6
Center Radius of First Mirror (in.)	23.88	21.53	19.23	16.98	14.78	12.63
Center Radius of Second Mirror (in.)	22.8273	20.5671	18.3590	16.2026	14.0971	12.0420
Center-to-Center Distance (in.)	35.0762	35.6091	36.0765	36.4822	36.8296	37.1223
Back Focal Distance (in.)	380	380	380	380	380	380
Grazing Angle at Center of each E1 (mrad)	15.0000	13.5178	12.0689	10.6531	9.2702	7.9197
Half-Width of Entrance Annulus (in.)	0.24	0.22	0.20	0.175	0.15	0.125
Image Curvature ($in.^{-1}$)	-0.262	-0.328	-0.417	-0.538	-0.730	-0.018
Focal Length (in.)	398.957	398.957	398.957	398.957	398.957	398.957

Front to Rear (see Figure 4a) - The undeformed Sagittal Cross-section is a circle with the radius ρ,

$$x^2 + y^2 = \rho^2 \quad . \tag{2}$$

An elliptical deformation can be described by

$$\frac{x^2}{(\rho + Q_1)^2} + \frac{y^2}{(\rho - Q_1)^2} = 1 \quad , \tag{3}$$

where Q_1 is the maximum deviation from the ideal circular cross-section. Equation 3 may be rearranged to

$$\frac{x^2}{(1 + Q_1/\rho)^2} + \frac{y^2}{(1 - Q_1/\rho)^2} = \rho^2$$

$$\text{or since } Q_1 \ll \rho \text{ and } \frac{\rho - \rho_0}{\rho_0} \ll 1 \quad ,$$

$$x^2 (1 - 2Q_1/\rho) + y^2 (1 + 2Q_1/\rho) = \rho^2 \quad . \tag{4}$$

Equation 4 inserted into the surface equation finally yields

$$x^2 (1 - 2Q_1/\rho) + y^2 (1 + 2Q_1/\rho) - \rho_0^2 = 2kz - (1 + \delta)z^2 \quad . \tag{5}$$

b) Elliptical Deformation with 90^0 Azimuthal Rotation from Front to Rear and Circular Cross-Section in the Middle (see Figure 4b) - This type of deformation occurs when a cylindrical element is squeezed at one end and was observed during the manufacturing process of the HEAO-B mirror elements. It can mathematically be described by replacing Q_1 in equation 5 with a product, one factor representing the maximum deviation at both ends and the other factor changing its values continuously from +1 at

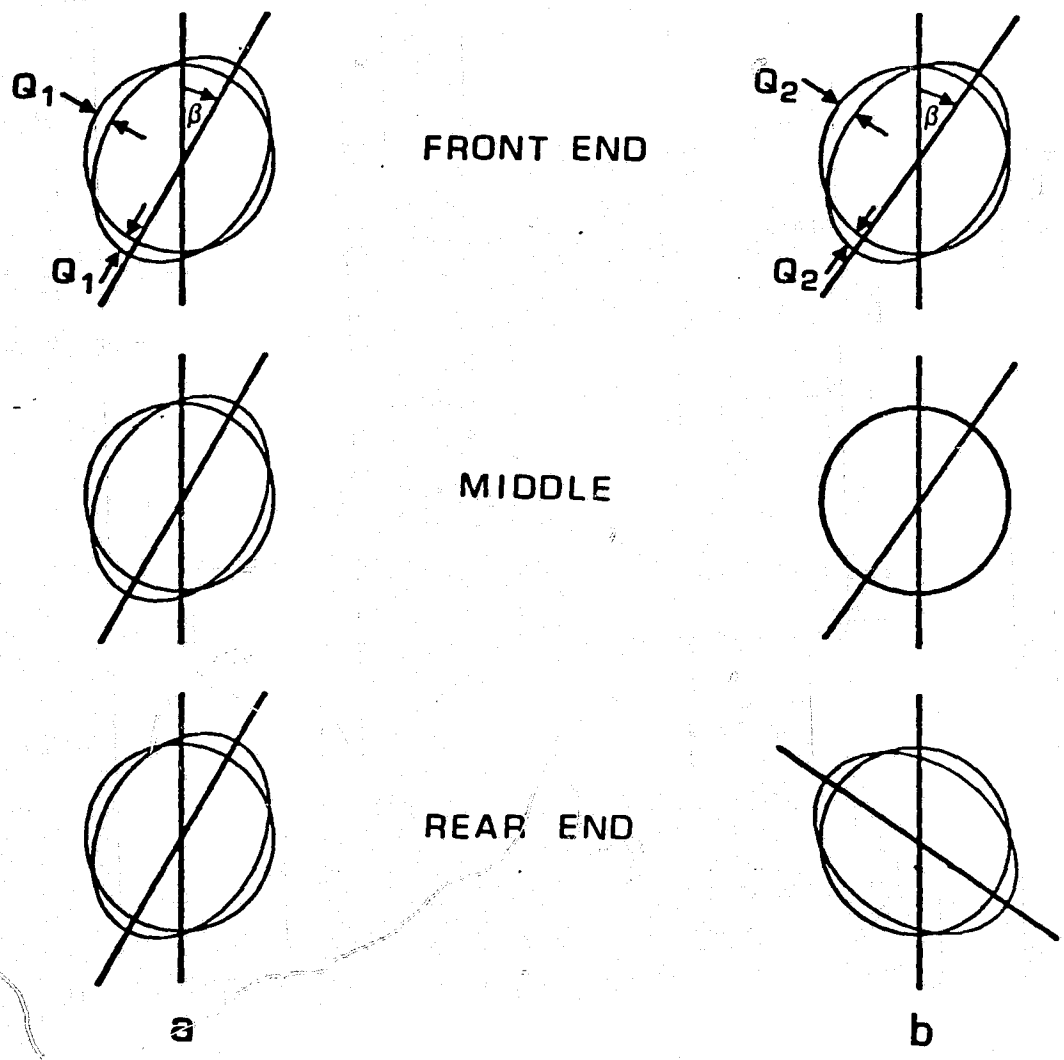

Fig. 4. Elliptical surface deformations: (a) constant orientation from front to rear end; (b) orientation at rear end orthogonal to orientation at front end. (The circles represent the undeformed cross-sections.)

the front to 0 in the middle and -1 at the rear of the element. Such a product is, for instance, given by

$$Q_2 \cdot \frac{z}{z_m} \quad ,$$

with the m in z_m designating maximum.

To maintain separation of the x,y-coordinates from th z-coordinate in the surface equation, we set

$$z \simeq (\rho^2 - \rho_0^2)/2k \quad \text{and} \quad z_m \simeq (\rho_m^2 - \rho_0^2)/2k \quad ,$$

which is an allowed approximation since the z^2 term in the original surface equation 1 is always very small. It then follows that

$$\frac{z}{z_m} \simeq \frac{\rho^2 - \rho_0^2}{2\rho_0 T} \quad ,$$

where $T = \rho_m - \rho_0$.

The surface equation for this deformation then becomes

$$x^2\left(1 - Q_2 \frac{\rho^2 - \rho_0^2}{T\rho_0^2}\right) + y^2\left(1 + Q_2 \frac{\rho^2 - \rho_0^2}{T\rho_0^2}\right) - \rho_0^2 = 2kz - (1+\delta)z^2 \quad . \qquad (6)$$

Sinusoidal Deformation of the Meridional Cross-Section (see Figure 5)

A sinusoidal deformation of the meridional section can be described by a sine function with an appropriate argument added to the radius, ρ,

in the original surface equation. Such a function is given by

$$q = Q_3 \cdot \sin\left(n\pi \frac{\rho^2 - \rho_0^2}{2T\,\rho_0} + \omega\right) \quad , \tag{7}$$

where Q_3 is the maximum deviation from the ideal cross-section, n determines the spatial frequency (number of periods per element length), and ω is the axial phase shift.

The surface equation then becomes

$$(\rho + q)^2 - \rho_0^2 = 2kz - (1 + \delta)\, z^2 \quad . \tag{8}$$

Since q is, per definition, a very small quantity, it is allowed to apply suitable approximations, resulting in

$$(\rho + q)^2 \simeq \rho^2 + 2\rho_0\, q \quad .$$

The surface equation for the sinuoidal deformation then becomes

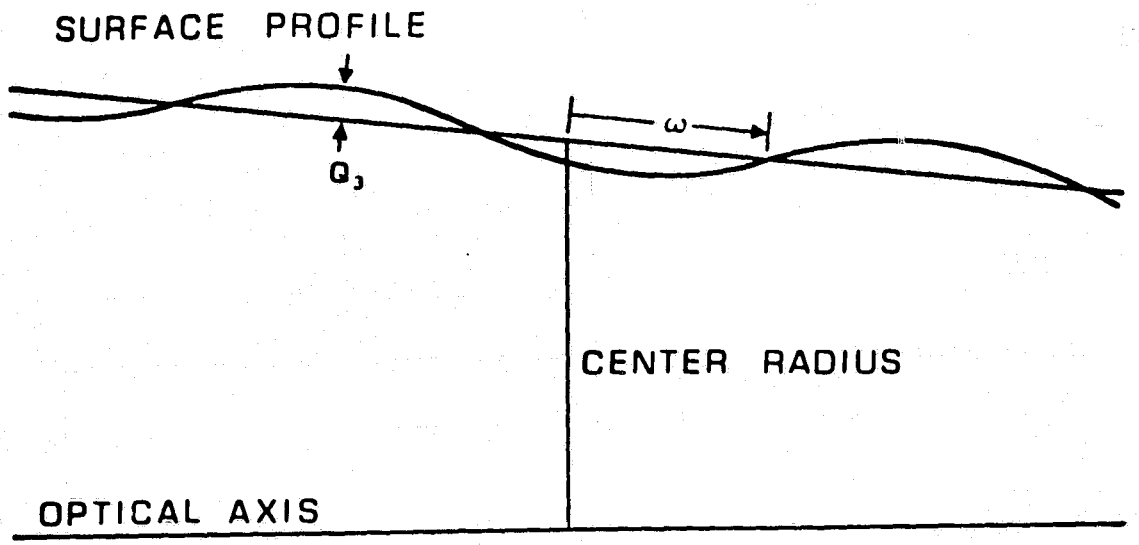

Fig. 5. Sinusoidal surface deformation.

$$\rho^2 - \rho_0^2 + 2\rho_0 Q_3 \cdot \sin\left(n\pi \frac{\rho^2 - \rho_0^2}{2T\rho_0} + \omega\right) = 2kz - (1+\delta)\, z^2 \quad . \tag{9}$$

Surface Deviation Due to Change of the Deformation Constant (See Fgiure 6)

A fourth form of surface deformation can be obtained by slightly changing the deformation constant, δ. This causes a lifting or lowering of the meridional section for $z \neq 0$ with maximum values at both ends of the element (see Figure 6). We determine the relation between the radial change and the variation of δ by deriving the surface equation

$$\rho^2 - \rho_0^2 = 2kz - (1+\delta)\, z^2 \quad ,$$

which yields

$$2\rho d\rho = -z^2 d\delta$$

or

$$d\delta = -\frac{2\rho}{z^2}\, d\rho \quad . \tag{10}$$

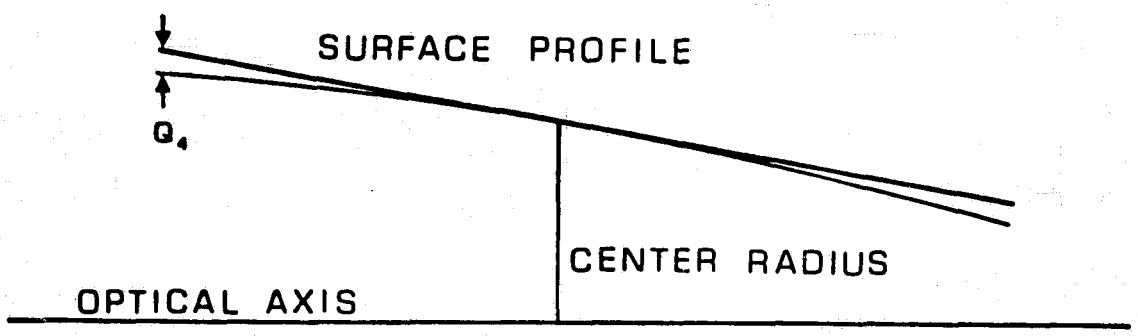

Fig. 6. Variation of deformation constant.

If the maximum deviation at the end (ρ_m, z_m) is $d\rho = Q_4$, equation 10 becomes

$$d\delta = -2Q_4 \frac{\rho_m}{z_m^2} \quad .$$

Since z_m is a parameter not used in the ray trace program, we replace it by using equation 1, neglecting again the z^2 term, and setting $\rho_m \simeq \rho_0$,

$$z_m \simeq \frac{\rho_m^2 - \rho_0^2}{2k} = \frac{(\rho_m + \rho_0)(\rho_m - \rho_0)}{2k} \simeq \frac{\rho_0 T}{k} \quad .$$

The surface equation for this type of deformation then becomes

$$\rho^2 - \rho_0^2 = 2kz - \left(1 + \delta - \frac{2k^2}{\rho_0 T^2} \cdot Q_4\right) z^2 \quad . \tag{11}$$

Combination of All Deformations

If we now combine all previously described deformations in a single surface equation, we obtain

$$\rho^2 - \rho_0^2 - \frac{2}{\rho_0}(x^2 - y^2)\left(Q_1 + Q_2 \frac{\rho^2 - \rho_0^2}{2\rho_0^2 T}\right) + 2Q_3 \rho_0 \cdot \sin\left(n\pi \frac{\rho^2 - \rho_0^2}{2\rho_0 T} + \omega\right) =$$

$$2kz - \left(1 + \delta - Q_4 \frac{2k^2}{\rho_0 T^2}\right) z^2 \tag{12}$$

where

Q_1 = elliptical deformation, same direction at both ends

Q_2 = elliptical deformation, orthogonal direction at both ends

Q_3 = amplitude of sinusoidal deformation

ω = axial phase shift of sinusoidal deformation

n = spatial frequency of sinusoidal deformation

Q_4= effective change of deformation constant.

Effects of Individual Defects on the Performance of a Single Two-Mirror System

Misalignments

Table 2 summarizes the sensitivities of the axial spot size to the different types of misalignments for each of the six subsystems. All spot sizes were established at the gaussian focal point.

Table 2. Misalignment sensitivities

		Despace	Decenter	Tilt
RMS-Spot Size Increase	System 1	0.015 μrad/μm	0.1 μrad/μm	1.9 μrad/μrad
	System 2	0.013 μrad/μm	0.1 μrad/μm	1.9 μrad/μrad
	System 3	0.012 μrad/μm	0.1 μrad/μm	1.9 μrad/μrad
	System 4	0.010 μrad/μm	0.1 μrad/μm	1.9 μrad/μrad
	System 5	0.09 μrad/μm	0.1 μrad/μm	1.9 μrad/μrad
	System 6	0.08 μrad/μm	0.1 μrad/μm	1.9 μrad/μrad

Of particular interest is the effect of combined tilt and decenter errors, because there is always one combination where these two errors cancel. Optimum cancellation can only be obtained when the direction of the decenter is orthogonal to the tilt axis. Figure 7 shows the axial spot size as a function of the tilt angle when combined with a constant decenter of 0.001 in. and different angles, ψ, between the tilt axis and the direction of decenter. It indicates the point of best cancellation on the 90^0 curve, but also shows that at the same point the misalignment

sensitivity (represented by the slope) reaches the maximum.

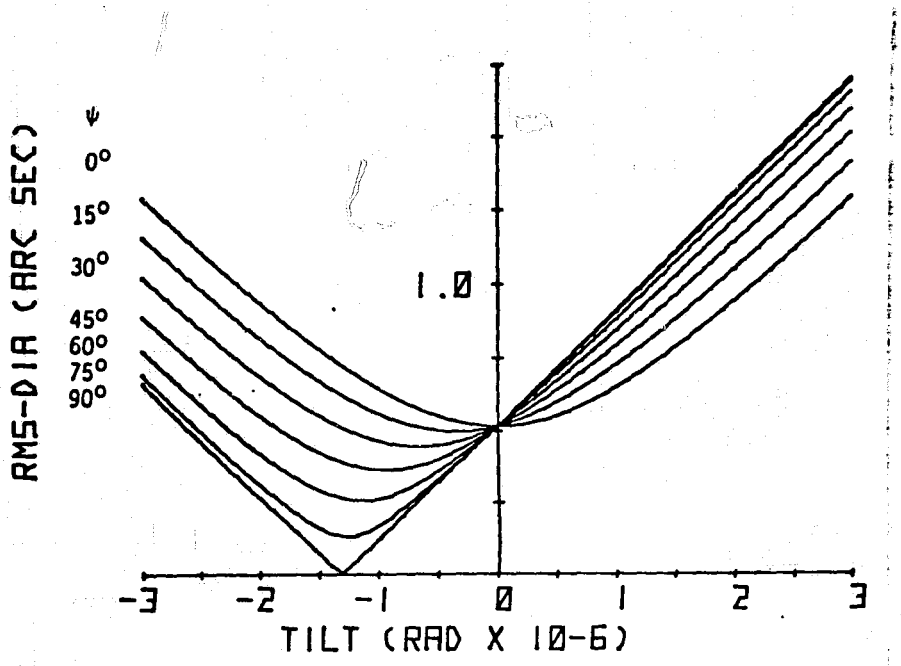

Fig. 7. The effect of tilt and decenter combination on the axial spot size for various angles, ψ, between direction of decenter and tilt axis. (Decenter = 0.001 in.)

Figure Errors

The effects of the individual figure errors as previously modeled on a single two-mirror system are presented in the following paragraphs. The design of the outer subsystem of the AXAF array served as example for this study.

Elliptical Deformation with Constant Orientation. Figure 8 shows the performance of the system with elliptically deformed elements. The orientation of the elliptical deformation in each element is constant. The axial rms-spot size is plotted against the azimuth angle, β, between the major axes of the deformation ellipses of both elements. A complete cancellation is achieved for orthogonal orientation.

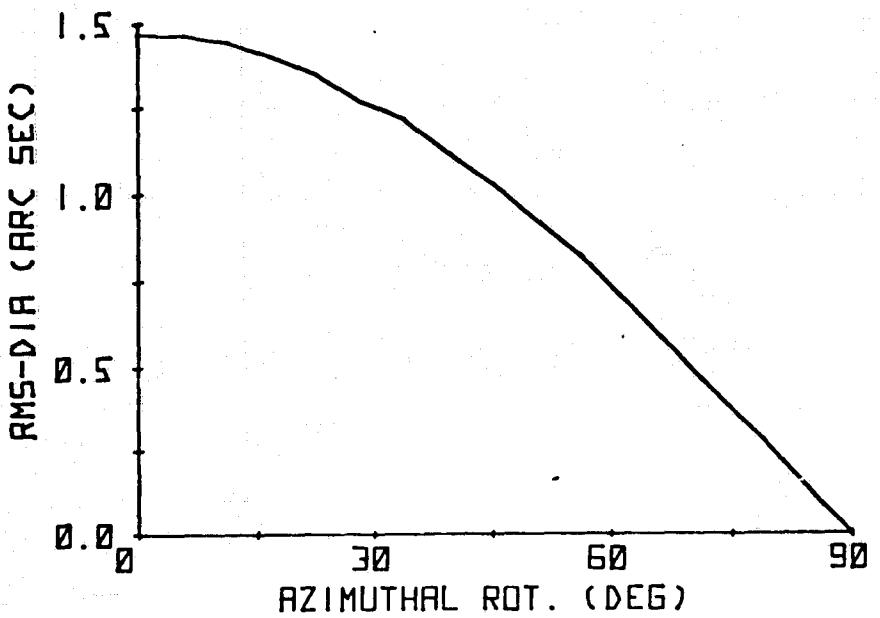

Fig. 8. The effects of uniform elliptical deformations on the axial spot size; the rms-spot size is plotted versus the azimuthal rotation of the secondary with respect to the primary for a maximum deformation of Q_1 = 0.001 in. on both surfaces.

Elliptical Deformation with 90^0 Change in Orientation. Figure 9 shows the performance of the system with elliptically deformed cross sections where the orientation of the major axis changes from front to rear. The axial rms-spot size is plotted against the azimuth angle, β, between the front major axes of the deformation ellipses of both elements. The best cancellation is obtained for the same orientation.

Sinusoidal Deformations. Figure 10 shows the axial spot size of the system with sinusoidal surface deformations. The axial rms-spot size is plotted against longitudinal shift of the pattern on the secondary with respect to that on the primary for various spatial frequencies, n. The plots were made for a constant maximum slope error of $\Delta\alpha = 0.5$ μrad. The relation between $\Delta\alpha$ and the maximum departure from the ideal surface figure, Q_3, is

$$Q_3 = z_m \Delta\alpha / n\pi \quad . \tag{13}$$

Figure Error Due to a Changed Deformation Constant, δ. Figure 11 shows the effects on the axial spot size caused by a change of the deformation constants. The deformation constant on the primary is constant with a corresponding $Q_4 = 5 \cdot 10^{-6}$ in., while Q_{42}, the error on the secondary, varied between 10^{-5} and 10^{-6} in.

We have tried to present a representative cross section of all figure errors investigated, although many more cases were studied. What we learned by studying the effects of individual errors on a single two-

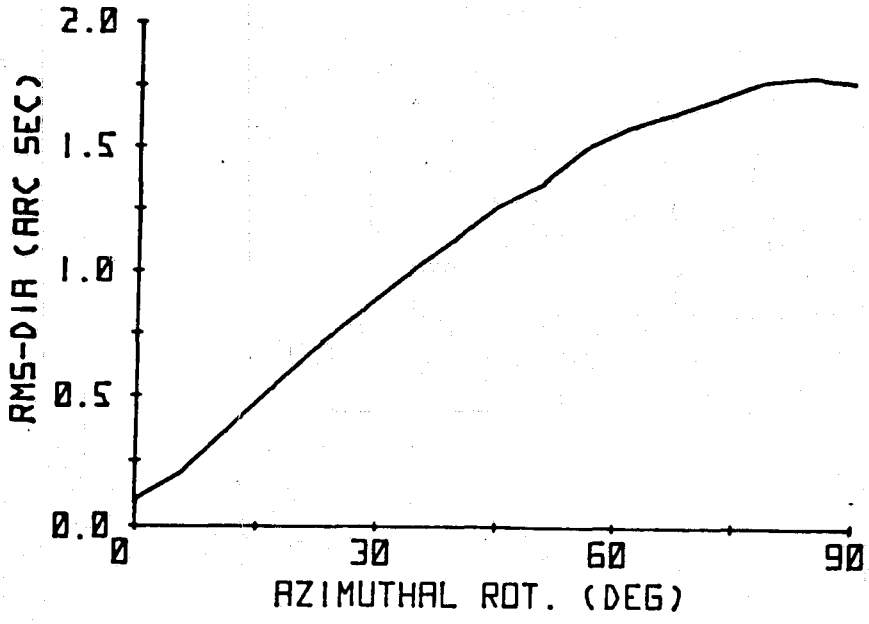

Fig. 9. The effect of orthogonal elliptical deformations on the axial spot size; the rms-spot size is plotted against the azimuthal rotation of the secondary with respect to the primary for a maximum of $Q_2 = 5 \cdot 10^{-5}$ in. on both surfaces.

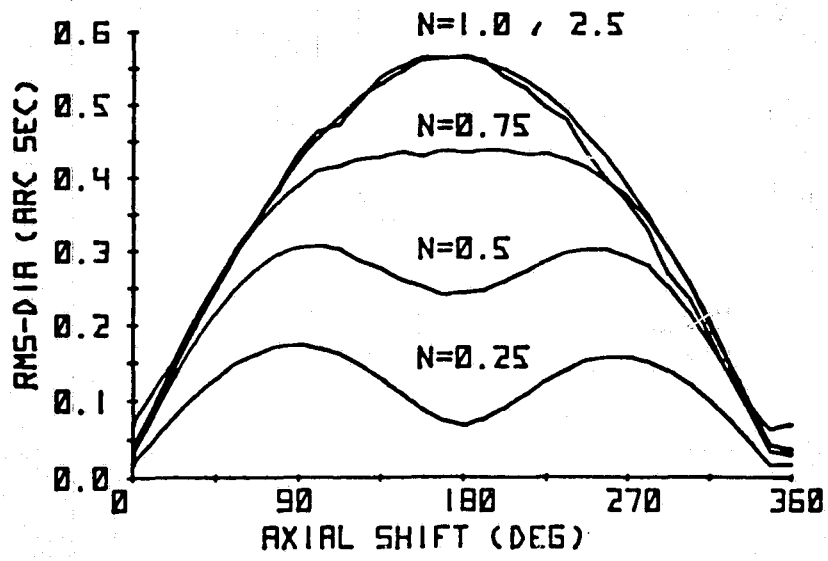

Fig. 10. The effects of sinusoidal surface deformations; the rms-spot size is plotted against the axial shift of the pattern on the secondary with respect to the primary for various spatial frequencies, N, and a constant maximum slope error of 0.5 μrad.

mirror system can be summarized as follows:

a) The main cause of image degradation due to figure errors is a change in slope.

b) If the figure error is of a sinusoidal nature, the spot size increases with the spatial frequency, n, for $n \leq 1$.

c) The effects of small aberrations behave linearly, and appropriate extrapolations are allowed.

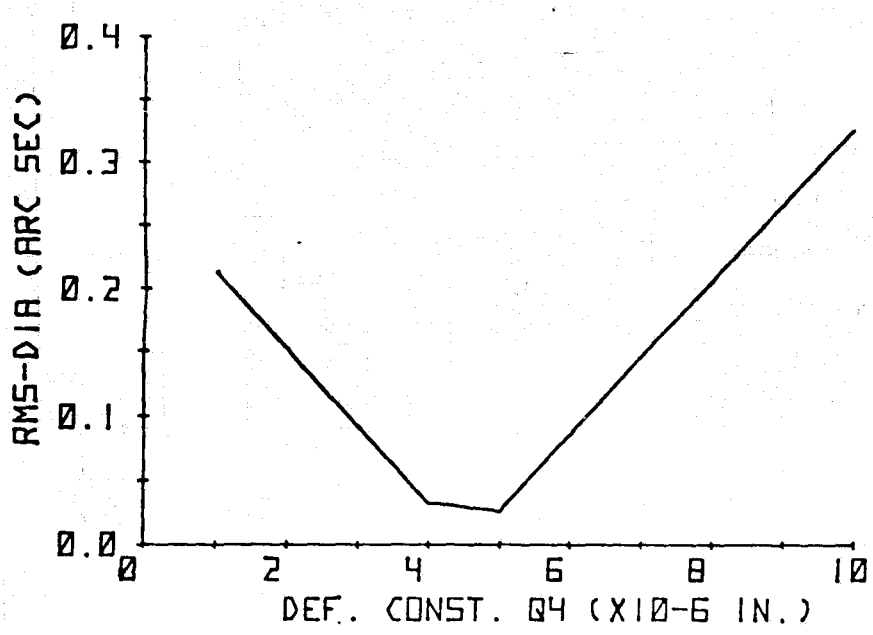

Fig. 11. The spot size is plotted against changing deformation constant on the secondary expressed by its maximum deviation Q_{42}; the change of the primary deformation is constant with its maximum deviation of $Q_{41} = 5 \cdot 10^{-6}$ in.

System Performance in the Presence of Alignment and Figure Errors

After determining the sensitivities of a single two-mirror system to various defects, the entire nested array was subjected to an error analysis. For this we consider three groups of errors:

a) Linear Misalignments (LM) - The LM's are displacements along the x-,y-, and z-axis.

b) Angular Misalignments (AM) - The AM's are tilts of an element about its center, O, in the x-, z-, and y,z-plane.

c) Figure Errors (FE) - The figure errors are modeled by combining ellipitcal and sinusoidal surface deformations as previously described.

To this purpose the actual surface deviations, Q_2 and Q_3, were expressed by their resulting slope errors, $\Delta\alpha_2$ and $\Delta\alpha_3$. The relations between Q_2 and $\Delta\alpha_2$, and Q_3 and $\Delta\alpha_3$ are given by

$$Q_2 = z_m \Delta\alpha_2 \qquad \text{and} \qquad Q_3 = z_m \Delta\alpha_3 \, n\pi \ .$$

The magnitudes of the individual errors are determined randomly within given upper and lower limits. For instance,

$$-10^{-4} \text{ in.} \leq \text{LM} \leq +10^{-4} \text{ in.}$$

means that each element may be displaced in three dimensions by an amount anywhere between -10^{-4} in. and $+10^{-4}$ in. per dimension.

The FE's are defined by their resulting maximum slope error, the frequency, n, and the phase, ω, of the sinusoidal deformation, and the azimuthal orientation, β, of the elliptical deformations. While the phase varies randomly from element to element, the spatial frequency is always 1 cycle per element length. The maximum slope error was generated

as follows:

$\Delta\alpha_2$ was a computer generated random number within the limits of

$$-5 \cdot 10^{-7} \leq \Delta\alpha_2 \leq 5 \cdot 10^{-7} \quad ,$$

and $\Delta\alpha_3$ was then calculated to be

$$\Delta\alpha_3 = (\text{sign of } \Delta\alpha_2) \cdot 5 \cdot 10^{-7} - \Delta\alpha_2 \quad ,$$

which results in a total slope error of

$$\Delta\alpha_2 + \Delta\alpha_3 = (\text{sign of } \Delta\alpha_2) \cdot 5 \cdot 10^{-7} \text{ rad} \quad .$$

One hundred computer runs for each set of errors were made to generate the probability curves of the expected telescope performance as shown in Figures 12 through 18. Figures 12 through 14 show the effects of linear and angular misalignments, individually and combined. Figures 15 and 16 give the performance curves in the presence of figure errors only, once for a fixed maximum slope error of $\pm 5 \cdot 10^{-7}$ rad on each mirror and secondly for a random total slope error within the limits of

$$-5 \cdot 10^{-7} \text{ rad} \leq \Delta\alpha_2 + \Delta\alpha_3 \leq +5 \cdot 10^{-7} \text{ rad} \quad .$$

Figures 17 and 18 give the expected performance in the presence of combined alignment and figure errors.

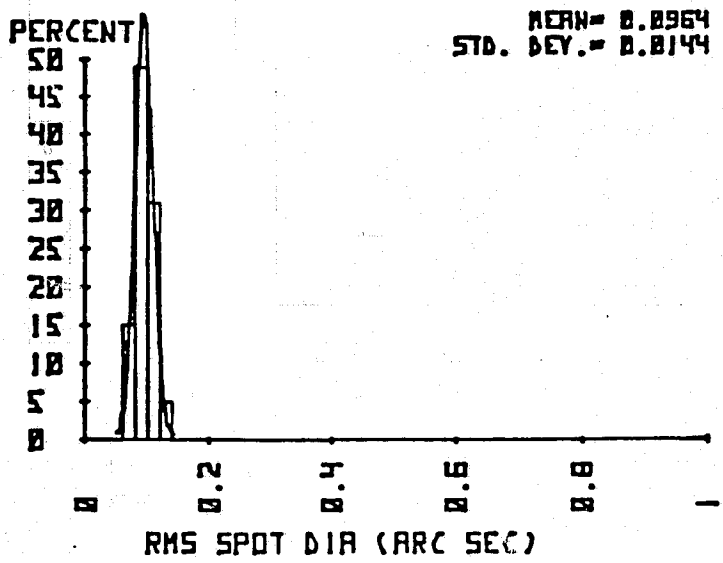

Fig. 12. Performance in the presence of linear misalignments only; -10^{-4} in. $\leq$ LM $\leq +10^{-4}$ in.

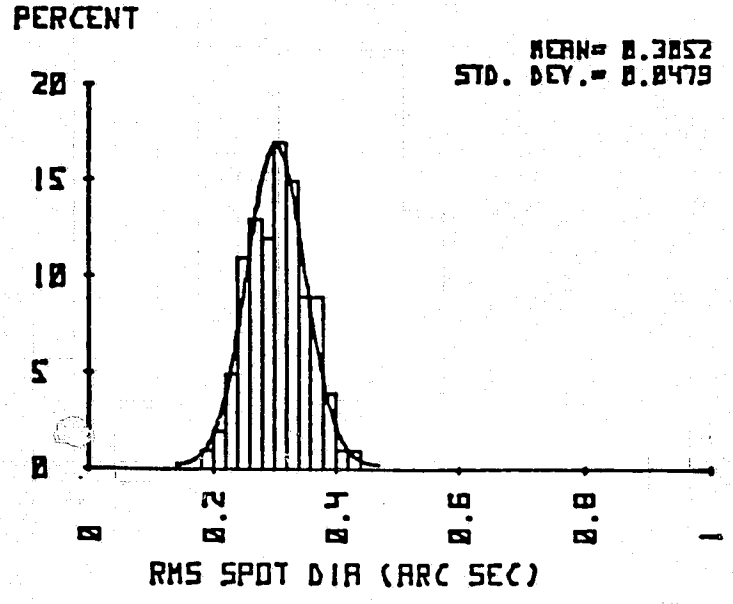

Fig. 13. Performance in the presence of angular misalignments only; $-5 \cdot 10^{-7}$ rad $\leq$ AM $\leq$ $+5 \cdot 10^{-7}$ rad.

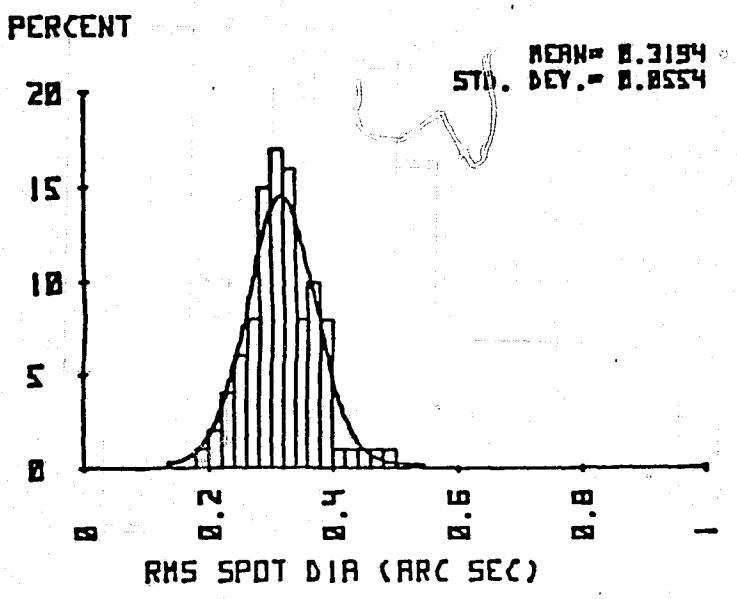

Fig. 14. Performance in the presence of linear and angular misalignments; -10^{-4} in. $\leq$ LM $\leq +10^{-4}$ in., $-5 \cdot 10^{-7}$ rad $\leq$ AM $\leq +5 \cdot 10^{-7}$ rad.

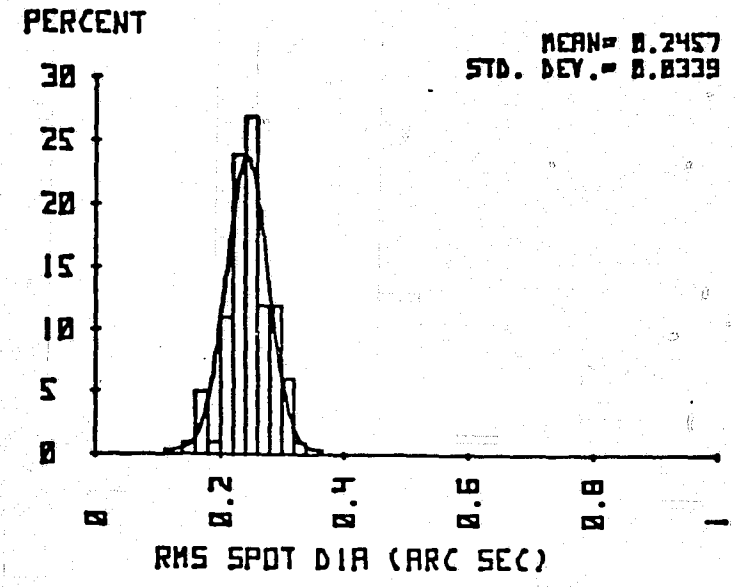

Fig. 15. Performance in the presence of figure errors only; $|FE| = 5 \cdot 10^{-7}$ rad.

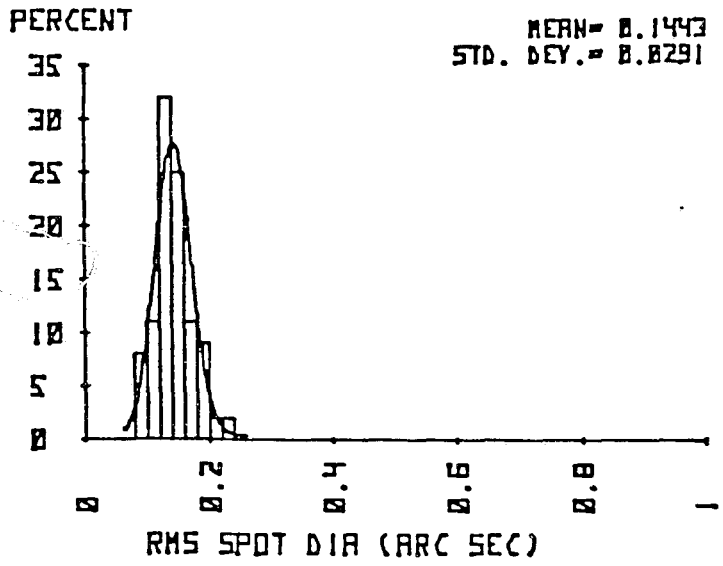

Fig. 16. Performance in the presence of figure errors only; $-5 \cdot 10^{-7}$ rad $\leq$ FE $\leq +5 \cdot 10^{-7}$ rad.

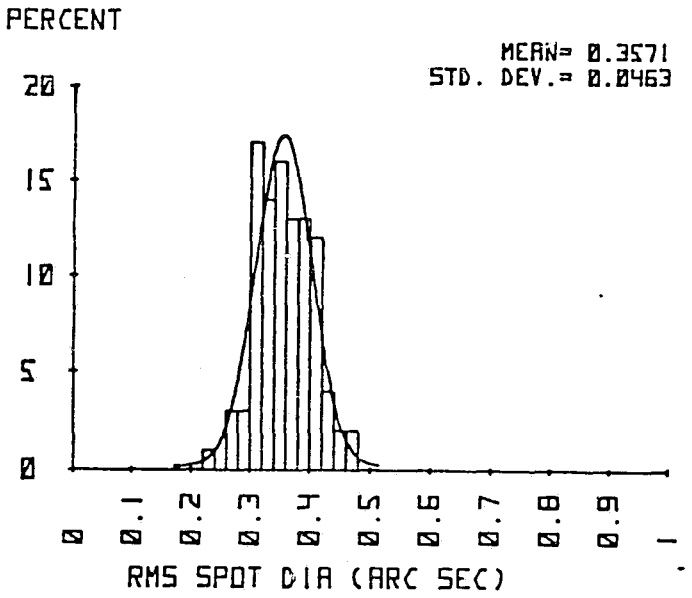

Fig. 17. Performance in the presence of alignment and figure errors; -10^{-4} in. $\leq$ LM $\leq +10^{-4}$ in., $-5 \cdot 10^{-7}$ rad $\leq$ AM $\leq +5 \cdot 10^{-4}$ rad, $-5 \cdot 10^{-7}$rad $\leq$ FE $\leq +5 \cdot 10^{-7}$ rad.

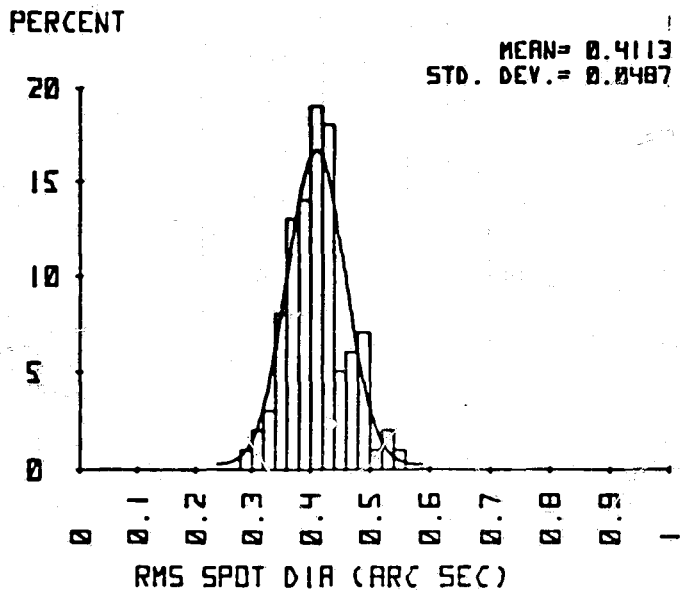

Fig. 18. Performance in the presence of alignment and figure errors; -10^{-4} in. $\leq$ LM $\leq +10^{-4}$ in., $-5 \cdot 10^{-7}$ rad $\leq$ AM $\leq +5 \cdot 10^{-7}$ rad, $|FE| = 5 \cdot 10^{-7}$ rad.

Conclusions

The analysis of the effects of alignment and figure errors on the performance of grazing incidence telescopes shows that the requirements for alignment accuracy and surface fidelity are extremely stringent when subsecond resolution is expected. The most sensitive defects are angular misalignments and slope errors. These errors, however, constitute only a part of the overall error budget that must also include performance degradation due to scattering instrument-related imperfections.

Reference

1. Dietrich Korsch, Analysis and Design Optimization of the 1.2m X-Ray Telescope, Final Report, NASA Contract NAS8-33158